ARTICLE

Background-free search for neutrinoless double-β decay of ^{76}Ge with GERDA

The GERDA Collaboration*

Many extensions of the Standard Model of particle physics explain the dominance of matter over antimatter in our Universe by neutrinos being their own antiparticles. This would imply the existence of neutrinoless double-β decay, which is an extremely rare lepton-number-violating radioactive decay process whose detection requires the utmost background suppression. Among the programmes that aim to detect this decay, the GERDA Collaboration is searching for neutrinoless double-β decay of ^{76}Ge by operating bare detectors, made of germanium with an enriched ^{76}Ge fraction, in liquid argon. After having completed Phase I of data taking, we have recently launched Phase II. Here we report that in GERDA Phase II we have achieved a background level of approximately 10^{-3} counts keV^{-1} kg^{-1} yr^{-1}. This implies that the experiment is background-free, even when increasing the exposure up to design level. This is achieved by use of an active veto system, superior germanium detector energy resolution and improved background recognition of our new detectors. No signal of neutrinoless double-β decay was found when Phase I and Phase II data were combined, and we deduce a lower-limit half-life of 5.3×10^{25} years at the 90 per cent confidence level. Our half-life sensitivity of 4.0×10^{25} years is competitive with the best experiments that use a substantially larger isotope mass. The potential of an essentially background-free search for neutrinoless double-β decay will facilitate a larger germanium experiment with sensitivity levels that will bring us closer to clarifying whether neutrinos are their own antiparticles.

One of the most puzzling aspects of cosmology is the unknown reason for the dominance of matter over antimatter in our Universe. Within the Standard Model of particle physics there is no explanation for this observation and hence a new mechanism has to be responsible. A favoured model called leptogenesis[1] links matter dominance to the nature of neutrinos and to the violation of lepton number—that is, the total number of electrons, muons, taus and neutrinos minus the number of their antiparticles.

In most extensions of the Standard Model[2-4], neutrinos are assumed to be their own antiparticles (that is, they are Majorana particles). This might lead to lepton-number-violating processes at the TeV energy scale observable at the LHC (Large Hadron Collider)[4] and would result in neutrinoless double-β ($0\nu\beta\beta$) decay where a nucleus of mass number A and charge Z decays as $(A, Z) \rightarrow (A, Z+2) + 2e^-$. Lepton number violation has not been unambiguously observed so far; indeed, its observation would motivate fundamental modifications of the Standard Model. There are several current experimental $0\nu\beta\beta$ decay programmes using, for example, ^{76}Ge (refs 5, 6), ^{130}Te (refs 7, 8) or ^{136}Xe (refs 9–11). They all measure the sum of the electron energies released in the decay, which corresponds to the mass difference $Q_{\beta\beta}$ of the two nuclei. The $0\nu\beta\beta$ decay half-life ($T_{1/2}^{0\nu}$) is at least 15 orders of magnitude longer than the age of the Universe. Its observation therefore requires the best suppression of backgrounds.

In the GERmanium Detector Array (GERDA) experiment, bare germanium detectors are operated in liquid argon (LAr). The detectors are made from germanium with the fraction of the ^{76}Ge isotope enriched from 7.8% to about 87%. Since the source and the detector of $0\nu\beta\beta$ decay are identical in this calorimetric approach, the detection efficiency is high.

This Article presents the first results from GERDA Phase II. In the first phase of data taking (Phase I), a limit of $T_{1/2}^{0\nu} > 2.1 \times 10^{25}$ yr (90% confidence level, CL) was found[5] for an exposure of 21.6 kg yr and a background rate of 0.01 counts keV^{-1} kg^{-1} yr^{-1} at $Q_{\beta\beta} = 2{,}039.061 \pm 0.007$ keV, called background index (BI) (ref. 12). At that

time, the result was based on data from 10 detectors (17.6 kg total mass). In December 2015, Phase II started with 37 detectors (35.6 kg) from enriched material. The mass is hence doubled relative to Phase I. The goal is an improvement of the half-life sensitivity to $>10^{26}$ yr for about 100 kg yr exposure by reducing the background index by an order of magnitude. The latter is achieved by vetoing background events through the detection of their energy deposition in the LAr and the characteristic time profile of their current signals in the germanium detectors. Up to the design exposure, the average expected background contribution is less than 1.0 in the energy region of interest ($Q_{\beta\beta} \pm 0.5$ full-width at half-maximum, FWHM), defined according to the FWHM energy resolution. This implies that GERDA is the first 'background-free' experiment in the field.

We will demonstrate here that GERDA has reached this target background level, which—if weighted by our superior energy resolution—is the best available at present. GERDA is therefore best suited to not only quote limits for a $0\nu\beta\beta$ decay but to identify such a signal with high confidence.

The experiment

The GERDA experiment[13] is located at the underground Laboratori Nazionali del Gran Sasso (LNGS) of INFN, Italy. A rock overburden of about 3,500 m water equivalent removes the hadronic components of cosmic ray showers and reduces the muon flux at the experiment by six orders of magnitude, to 1.2 muons m^{-2} h^{-1}.

The pioneering feature of GERDA is the operation of bare germanium detectors in a radiopure cryogenic liquid (LAr), which both cools the detectors to their operating temperature of about 90 K and shields them from external radiation originating from the walls (see Extended Data Fig. 1 for a sketch of the set-up)[14]. The 64 m^3 LAr cryostat is inside a 590 m^3 water tank, and the clean water completes the passive shield. Above the water tank is a clean room with a glove box and lock, used for the assembly of germanium detectors into strings and the integration of the LAr veto system (see below).

GERDA deploys 7 coaxial detectors from the former Heidelberg-Moscow[15] and IGEX[16] experiments, and also 30 Broad Energy germanium (BEGe) detectors[17]. All are produced from p-type material (see Extended Data Fig. 2). Electron–hole pairs created in the 1–2-mm-thick n+ electrode mostly recombine such that the active volume is reduced. The BEGe detectors provide a better identification of the event topology and hence background rejection (see below). The enriched detectors are assembled into six strings, which surround the central string; the central string consists of three coaxial detectors made from germanium of natural isotopic composition. Each string is placed inside a nylon cylinder (see Extended Data Fig. 3) to limit the LAr volume from which radioactive ions like ^{42}K can be collected on the outer detector surfaces[18,19].

All detectors are connected to custom-made low radioactivity charge sensitive amplifiers[20] (30 MHz bandwidth, 0.8 keV FWHM resolution) located in the LAr about 35 cm above the detectors. The charge signal traces are digitized with a 100 MHz sampling rate and stored on disk for offline analysis.

In background events, some energy is often also deposited in the argon. The resulting scintillation light[21] can be detected to veto these events, that is, to remove them from the analysis. In Phase II, a cylindrical volume of 0.5 m diameter and 2.2 m height around the detector strings (see Extended Data Figs 1 and 4) is instrumented with light sensors. The central 0.9 m of the cylinders is defined by a curtain of wavelength-shifting fibres which surround the 0.4-m-high detector array. The fibres are read out at both ends with 90 silicon photomultipliers (SiPMs)[22]. Groups of six 3×3 mm^2 SiPMs are connected together to a charge sensitive amplifier. Sixteen 3-inch low-background photomultipliers (PMTs) designed for cryogenic operation are mounted at the top and bottom surfaces of the cylindrical volume. Their distance to any germanium detector is at least 0.7 m to limit the PMT background contribution from their intrinsic Th/U radioactivity. All LAr veto channels are digitized and read out together with the germanium channels if at least one detector has an energy deposition above about 100 keV.

The nylon cylinders, the fibres, the PMTs and all surfaces of the instrumented LAr cylindrical volume are covered with a wavelength shifter to shift the LAr scintillation light from 128 nm to about 400 nm to match the peak quantum efficiency of the PMTs and the absorption maximum of the fibres. The water tank is instrumented with 66 PMTs to detect Cherenkov light from muons passing through the experiment. On top of the clean room are three layers of plastic scintillator panels covering the central 4×3 m^2 to complete the muon veto[23].

Data analysis

The data analysis flow is very similar to that of Phase I. The offline analysis of the digitized germanium signals is described elsewhere[5,24,25]. A data blinding procedure is again applied; events with a reconstructed energy in the interval $Q_{\beta\beta} \pm 25$ keV are not analysed but only stored on disk. After the entire analysis procedures and parameters have been frozen, these blinded events are processed.

The gain stability of each germanium detector is continuously monitored by injecting charge pulses (test pulses) into the front-end electronics at a rate of 0.05 Hz. The test pulses are also used to monitor leakage current and noise. Only data recorded during stable operating conditions (for example, with a gain stability better than 0.1%) are used for the physics analysis. This corresponds to about 85% of the total data written on disk.

Signals originating from electrical discharges in the high voltage line or bursts of noise are rejected during the offline event reconstruction by a set of multi-parametric cuts based on the flatness of the baseline, polarity and time structure of the pulse. Physical events at $Q_{\beta\beta}$ are accepted with an efficiency greater than 99.9%, estimated from γ lines in calibration data, test pulse events and template signals injected in the data set. Conversely, a visual inspection of all events above 1.6 MeV shows that no unphysical event survives the cuts.

The energy deposited in a germanium detector is reconstructed offline with an improved digital filter[26], whose parameters are optimized for each detector and for several periods. The energy scale and resolution are determined with weekly calibration runs with ^{228}Th sources. The long-term stability of the scale is assessed by monitoring the shift of the position of the 2,615 keV peak between consecutive calibrations. It is typically smaller than 1 keV for BEGe detectors and somewhat worse for some coaxial ones. The FWHM resolution at 2.6 MeV is 2.6–4.0 keV (mean 3.2 keV, r.m.s. 0.4 keV) for the BEGe detectors and 3.4–4.4 keV (mean 3.8 keV, r.m.s. 0.3 keV) for the coaxial detectors. The width of the strongest γ lines in the physics data (1,460 keV from ^{40}K and 1,525 keV from ^{42}K) is found to be 0.5 keV larger than expected for the coaxial detectors (see Fig. 1), probably owing to gain instabilities in the corresponding readout channels between calibrations. In order to conservatively estimate the expected energy resolution at $Q_{\beta\beta}$, an additional noise term is added to take this into account.

For $0\nu\beta\beta$ decays in the active part of a detector volume, the total energy of $Q_{\beta\beta}$ is detected in that detector in 92% of the cases. Multiple detector coincidences are therefore discarded as background events. Two consecutive candidate events within 1 ms are also rejected (dead time $\sim 10^{-4}$) to discriminate time-correlated decays from primordial radioisotopes, such as the radon progenies ^{214}Bi and ^{214}Po. Candidate events are also rejected if a muon trigger occurred within 10 μs before a germanium detector trigger. More than 99% of the muons that deposit energy in a germanium detector are rejected this way. The induced dead time is <0.1%.

The traces from PMTs and SiPMs are analysed offline to search for LAr scintillation signals in coincidence with a germanium detector trigger. An event is rejected if any of the light detectors record a signal of amplitude above 50% of the expectation for a single photo-electron within 5 μs from the germanium trigger. About 99% of the photons occur in this window. Accidental coincidences between the LAr veto system and germanium detectors create a dead time of $(2.3 \pm 0.1)\%$ which is measured with test pulse events and cross-checked with the counts in the ^{40}K peak. As the 1,460 keV γ is produced by electron capture of ^{40}K, there is no residual energy that can be released in the LAr volume.

Figure 2 shows the energy spectra for BEGe and coaxial detectors of Phase II with and without the LAr veto cut. Below about 500 keV the spectra are dominated by ^{39}Ar β decays, up to 1.7 MeV they are dominated by events from double-β decay with two neutrino emission ($2\nu\beta\beta$), above 2.6 MeV they are dominated by α decays on the detector surface, and around $Q_{\beta\beta}$ they are largely a mixture of α events, ^{42}K β decays and events from the decays of the ^{238}U and ^{232}Th chains. The two spectra (Fig. 2a and b) are similar except for the number of α events, which is on average higher for coaxial detectors. The number of α counts shows a large variation between the detectors. The power of the LAr veto is best demonstrated by the ^{42}K line at 1,525 keV, which is suppressed by a factor ~ 5 (Fig. 2b inset) owing to the β particle depositing energy up to 2 MeV in the LAr. Figure 2a and b also shows the predicted $2\nu\beta\beta$ spectrum from ^{76}Ge using our Phase I result for the half-life, $T_{1/2}^{2\nu} = (1.926 \pm 0.094) \times 10^{21}$ yr (ref. 27).

The time profile of the germanium detector current signal is used to discriminate $0\nu\beta\beta$ decays from background events. While the former have point-like energy deposition in the germanium (single site events, SSEs), the latter have often multiple depositions (multi-site events, MSEs) or depositions on the detector surface. The same pulse shape discrimination (PSD) techniques of Phase I are applied[28]. Events in the double escape peak (DEP) and at the Compton edge of 2,615 keV photons in calibration data have a similar time profile to $0\nu\beta\beta$ decays and are hence proxies for SSEs. These samples are used to define the PSD cuts and the related detection efficiencies. The latter are cross-checked with $2\nu\beta\beta$ decays.

The geometry of the BEGe detectors allows the application of a simple mono-parametric PSD based on the maximum of the detector current pulse A normalized to the total energy E (refs 29, 30). The
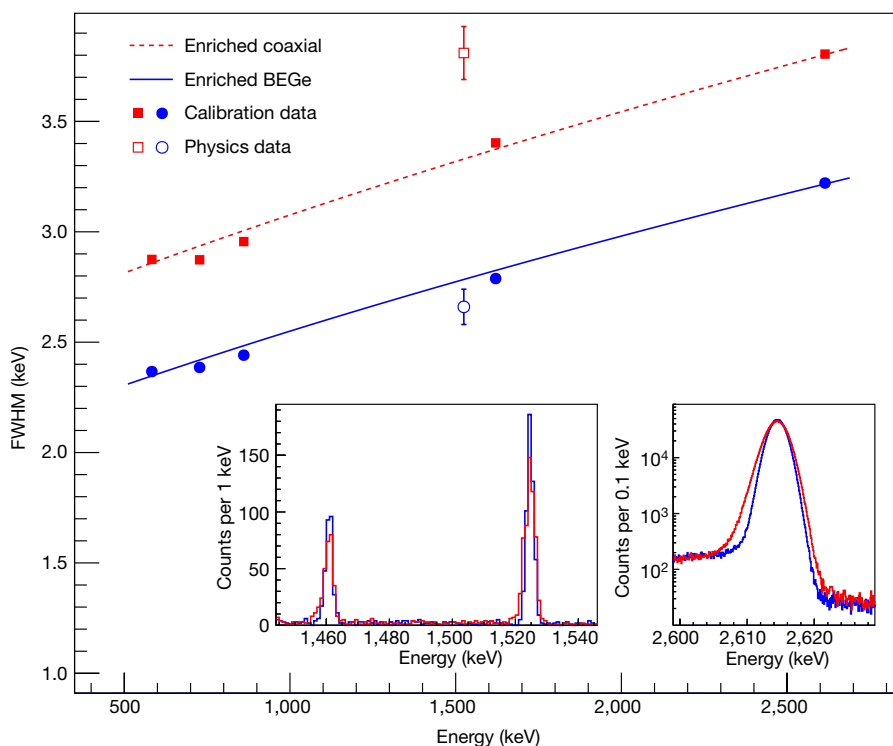
Figure 1 | Energy scale and resolution. Average energy resolution (FWHM) for γ lines of the calibration spectrum (filled symbols) and for the average of ^{40}K and ^{42}K lines from physics data (open symbols) for BEGe (symbols and solid line in blue) and coaxial (symbols and dashed line in red) detectors; error bars (± 1 s.d.) are derived from the fit. Insets show the spectrum of physics data in the energy region around the potassium lines (left) and the spectrum of the 2,615 keV calibration peak (right).

energy dependence of the mean and the resolution σ_{ae} of A/E are measured for every detector with calibration events. After correcting for these dependences and normalizing the mean A/E of DEP events to 1, the acceptance range is determined for each detector individually: the lower cut is set to keep 90% of DEP events and the upper position is twice the low-side separation from 1. Figure 3a shows a scatter plot of the PSD parameter $\zeta = (A/E - 1)/\sigma_{ae}$ versus energy. Accepted SSE-like events around $\zeta = 0$ are marked in red. Figure 3b displays the

energy spectrum before and after PSD selection. A survival fraction of $85^{+2}_{-1}\%$ is determined for $2\nu\beta\beta$ events which dominate the low energy part of the spectrum. The two potassium peaks and Compton scattered photons are reconstructed at $\zeta < 0$. All 234 α events at higher energies exhibit $\zeta > 0$ and are easily removed. The average $0\nu\beta\beta$ survival fraction is[31] $(87 \pm 2)\%$. The uncertainty takes into account the systematic difference between the A/E centroids of DEP and $2\nu\beta\beta$ events, and the different fractions of MSEs in DEP and $0\nu\beta\beta$ events.
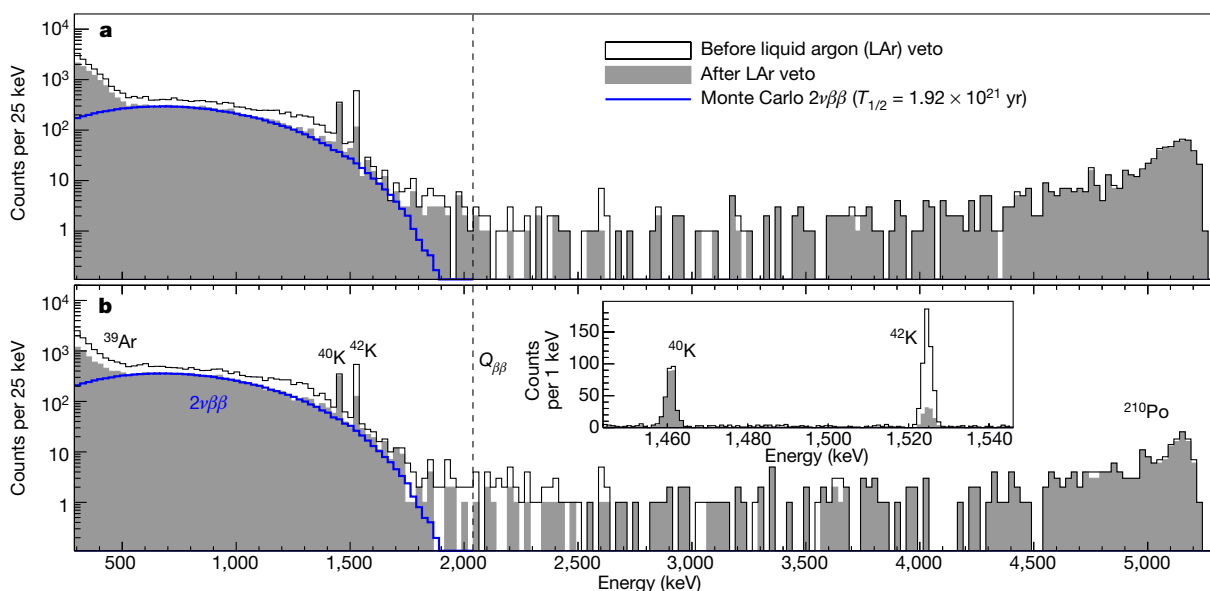

Figure 2 | Energy spectra for the two detector types. Energy spectra of Phase II data sets before (open histogram) and after (filled histogram) the argon veto cut, for **a**, the enriched coaxial detectors (exposure 5.0 kg yr), and **b**, the enriched BEGe detectors (exposure 5.8 kg yr). The blue lines are the expected $2\nu\beta\beta$ spectra from our recent half-life measurement. Inset, the BEGe spectrum in the energy region around the two potassium lines. We note that the ^{40}K line is not suppressed since no energy is deposited in the LAr. Various background contributions are labelled in **b**.
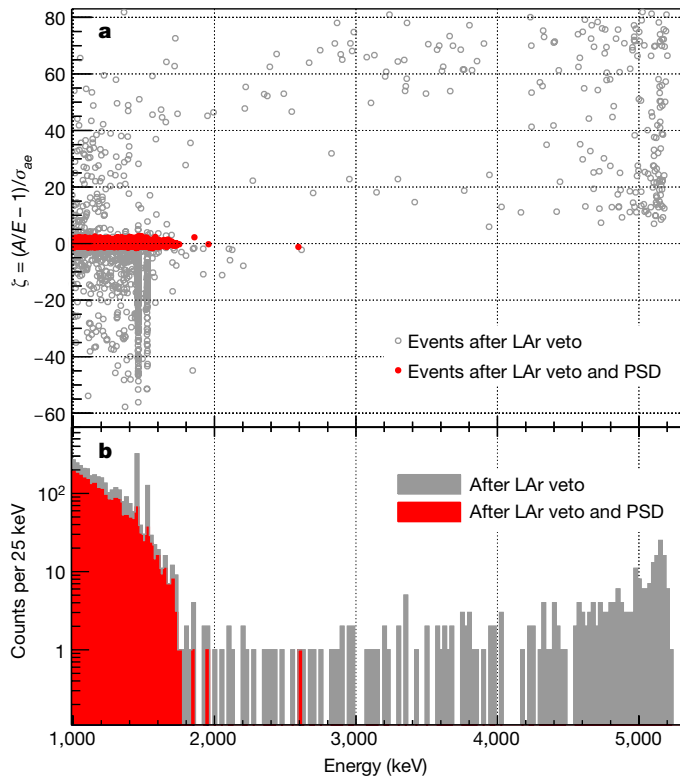
Figure 3 | Pulse shape discrimination. For all enriched BEGe detectors (exposure 5.8 kg yr) in Phase II: **a**, plot of PSD parameter $\zeta = (A/E - 1)/\sigma_{ae}$ versus energy for physics data, and **b**, the energy spectrum for the same event sample. Red circles (**a**) and red spectrum (**b**) represent events that pass the selection. Because the cuts are detector specific, the accepted ζ ranges differ.

For coaxial detectors, a mono-parametric PSD is not sufficient because SSEs do not have a simple signature[28]. Instead, two neural network algorithms are applied to discriminate SSEs from MSEs and from α surface events. The first neural network algorithm is identical to the one used in Phase I. The cut on the neural network qualifier is set to yield a survival fraction of DEP events of 90% for each detector. For the determination of the $0\nu\beta\beta$ efficiency, $2\nu\beta\beta$ events in physics data and a complete Monte Carlo simulation[32] of physics data and calibration data are used. The simulation considers the response of the detector and the electronics to energy depositions including the drift of charges in the crystal[33]. We find a survival fraction for $0\nu\beta\beta$ events of $(85 \pm 5)\%$, where the uncertainty is derived from variations of the simulation parameters.

The second neural network algorithm is applied for the first time, and identifies surface events on the p+ electrode. Training of this algorithm is done with physics data from two different energy intervals. After the LAr veto cut, events in the range 1.0–1.3 MeV are almost exclusively from $2\nu\beta\beta$ decay and hence signal-like. Events above 3.5 MeV are almost all from α decays on the p+ electrode, and represent background events in the training. Analysing a $2\nu\beta\beta$ event sample not used in the training we estimate a $0\nu\beta\beta$ efficiency of $(93 \pm 1)\%$. The combined PSD efficiency for coaxial detectors is $(79 \pm 5)\%$.

Results

This analysis includes the data sets used in the previous publication[5,34], an additional coaxial detector period from 2013 ('PI extra' in Table 1) and the Phase II data from December 2015 until June 2016 ('PIIa coaxial' and 'PIIa BEGe' in Table 1). Table 1 lists the relevant parameters for all data sets. The exposures in the active volumes of the detectors for ^{76}Ge are 234 mol yr and 109 mol yr for Phases I and II, respectively. The efficiency ϵ is the product of the ^{76}Ge isotope fraction (87%), the active

Table 1 | Parameters of data sets

Data set	$\mathcal{E}$ (kg yr)	FWHM (keV)	ϵ	BI (10^{-3} counts keV^{-1} kg^{-1} yr^{-1})
PI golden	17.9	4.3(1)	0.57(3)	11 ± 2
PI silver	1.3	4.3(1)	0.57(3)	30 ± 10
PI BEGe	2.4	2.7(2)	0.66(2)	5^{+4}_{-3}
PI extra	1.9	4.2(2)	0.58(4)	5^{+4}_{-3}
PIIa coaxial	5.0	4.0(2)	0.53(5)	$3.5^{+2.1}_{-1.5}$
PIIa BEGe	5.8	3.0(2)	0.60(2)	$0.7^{+1.1}_{-0.5}$

List of data sets, exposures $\mathcal{E}$ (for total mass), energy resolutions in FWHM, efficiencies ϵ (including enrichment, active mass, selection efficiencies and dead times) and background indices (BI) in the analysis window excluding $Q_{\beta\beta} \pm 5$ keV. The numbers in parenthesis give the uncertainty of the respective values in the least significant digit.

volume fraction (87%–90%), the $0\nu\beta\beta$ event fraction reconstructed at full energy in a single crystal (92%), pulse shape selection (79%–92%) and the live time fraction (97.7%). For the Phase I data sets the event selection including the PSD classification is unchanged. An improved energy reconstruction[26] is applied to the data as well as an updated value for the coaxial detector PSD efficiency of the neural network analysis of $(83 \pm 3)\%$ (ref. 32).

Figure 4 shows the spectra for the combined Phase I data sets and the two Phase II sets. The analysis range is from 1,930 keV to 2,190 keV excluding the intervals $2,104 \pm 5$ keV and $2,119 \pm 5$ keV, which correspond to known peaks predicted by our background model[18]. For the Phase II coaxial detectors, four events survive the cuts which means that the background is reduced by a factor of three compared to Phase I (see 'PI golden' in Table 1). Owing to the better PSD performance, only one event remains in the BEGe data which corresponds to a background index of $0.7^{+1.1}_{-0.5} \times 10^{-3}$ counts keV^{-1} kg^{-1} yr^{-1}. Consequently, the Phase II background goal has been reached.

The statistical analysis is described in Methods. We perform both a frequentist and a Bayesian analysis based on an unbinned extended likelihood function[34]. The fit function for every data set is a flat distribution for the background (one free parameter per data set) and for a possible signal a Gaussian centred at $Q_{\beta\beta}$ with a width according to the corresponding resolution listed in Table 1. The signal strength is calculated for each set according to its exposure, efficiency and the inverse half-life $1/T$ which is a common free parameter. The analysis accounts for the systematic uncertainties due to efficiencies and energy resolutions (see Table 1), and to a possible offset in the energy scale.

The P-value distribution for the frequentist analysis is shown in Extended Data Fig. 5. The best fit yields zero signal events, with a 90% CL limit of 2.0 events in 34.4 kg yr total exposure or:

$$T^{0\nu}_{1/2} > 5.3 \times 10^{25} \text{ yr} \qquad (1)$$

The (median) sensitivity assuming no signal is 4.0×10^{25} yr. The systematic uncertainties weaken the limit by <1%. The Bayesian fit yields, for a prior flat in $1/T$ between 0 and 10^{-24} yr^{-1}, a limit of $T^{0\nu}_{1/2} > 3.5 \times 10^{25}$ yr (90% CI). The sensitivity assuming no signal is 3.1×10^{25} yr.

Discussion

GERDA Phase II has been taking data since December 2015 in stable conditions with all channels working. The background index at $Q_{\beta\beta}$ for the BEGe detectors is BI $= (0.7^{+1.1}_{-0.5}) \times 10^{-3}$ counts keV^{-1} kg^{-1} yr^{-1}. This is a substantial achievement, as the value is consistent with our design goal. We find no hint of a $0\nu\beta\beta$ decay signal in our combined data, and place a limit of $T^{0\nu}_{1/2}(^{76}\text{Ge}) > 5.3 \times 10^{25}$ yr (90% CL, sensitivity 4.0×10^{25} yr). For light Majorana neutrino exchange and a nuclear matrix element range for ^{76}Ge between 2.8 and 6.1 (refs 35–41), the GERDA half-life limit converts to a limit on the effective Majorana neutrino mass of $m_{\beta\beta} < 0.15$–0.33 eV (90% CL).

The mean expected background is 0.8 in the energy region of interest at the design exposure of 100 kg yr: that is, a background of
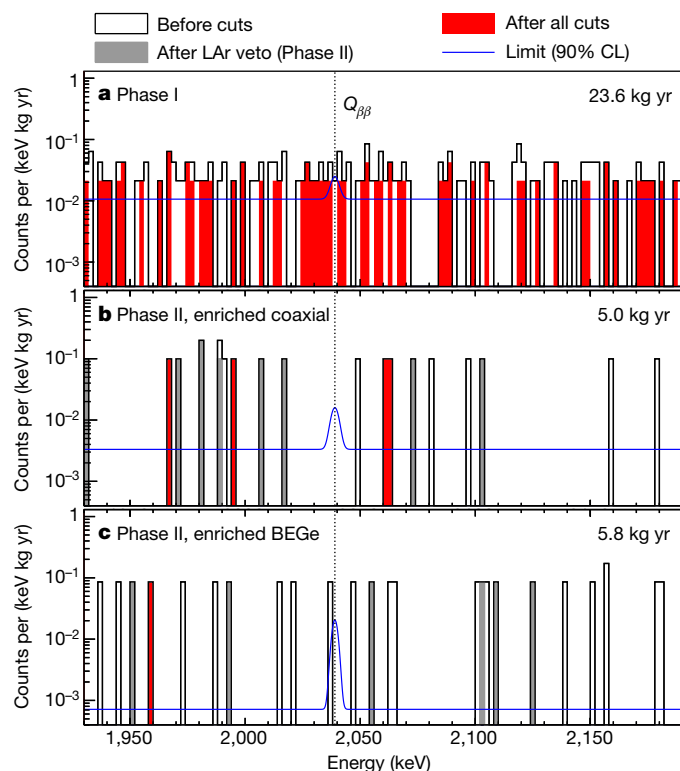
Figure 4 | Energy spectra in the analysis window around $Q_{\beta\beta}$. Shown are combined Phase I data (**a**), Phase II coaxial detector spectra (**b**) and Phase II BEGe detector spectra (**c**) in the analysis window. The binning is 2 keV; the exposures are given in the panels at top right. The open histogram is the spectrum before the PSD and LAr veto cut, the filled grey one shows the spectrum after the LAr veto (applies only to Phase II), and the red histogram is the final spectrum after LAr veto and PSD. The blue line represents the fitted spectrum together with a hypothetical signal corresponding to the 90% CL limit of $T_{1/2}^{0\nu} = 5.3 \times 10^{25}$ yr.

less than one. GERDA is hence the first 'background-free' experiment in the field. The sensitivity of such a background-free experiment grows approximately linearly with exposure, unlike the sensitivity of competing experiments that grows with the square root of exposure. GERDA will reach a sensitivity of the order of 10^{26} yr for the half-life within 3 years of continuous operation. With the same exposure we have a 50% chance of detecting a signal with 3σ significance if the half-life is almost 10^{26} yr.

Phase II has demonstrated that the concept of background suppression by exploiting the good pulse shape performance of BEGe detectors and by detecting the argon scintillation light works. The background at $Q_{\beta\beta}$ is the best available at present: it is lower by a factor of typically 10 compared to experiments using other isotopes after normalization by the energy resolution and total efficiency ϵ, that is, our value of (BI × FWHM)/ϵ is superior. This is why the GERDA half-life sensitivity of 4.0×10^{25} yr for an exposure of 343 mol yr is similar to that of the Kamland-Zen experiment obtained using ^{136}Xe, that is, 5.6×10^{25} yr based on a more than tenfold exposure of 3,700 mol yr (ref. 9).

A discovery of $0\nu\beta\beta$ decay would have far-reaching consequences for our understanding of particle physics and cosmology. Key features of a convincing discovery would include an ultra-low background with a simple flat distribution, excellent energy resolution and the possibility of identifying the events with high confidence as signal-like as opposed to being an unknown γ line from a nuclear transition. The last is achieved by detector pulse shape analysis and possibly by a signature in the argon. Bare germanium detectors in liquid argon, as used in GERDA, give the best chance of a discovery, which has motivated future extensions of the programme. The GERDA cryostat can hold 200 kg of detectors; such an experiment will remain 'background-free'

until an exposure of 1,000 kg yr, provided that the background can be further reduced by a factor of five. The discovery sensitivity would then improve by an order of magnitude to a half-life of 10^{27} yr. The 200 kg set-up is conceived as a first extension towards a more ambitious 1 ton experiment, which would ultimately boost the sensitivity to 10^{28} yr corresponding to the $m_{\beta\beta} < 10$–20 meV range. Both extensions are being pursued by the newly formed LEGEND Collaboration (http://www.legend-exp.org).

Online Content Methods, along with any additional Extended Data display items and Source Data, are available in the online version of the paper; references unique to these sections appear only in the online paper.

1. Davidson, S., Nardi, E. & Nir, Y. Leptogenesis. *Phys. Rep.* **466,** 105–177 (2008).
2. Mohapatra, R. N. & Smirnov, A. Y. Neutrino mass and new physics. *Annu. Rev. Nucl. Part. Sci.* **56,** 569–628 (2006).
3. Mohapatra, R. N. *et al.* Theory of neutrinos: a white paper. *Rep. Prog. Phys.* **70,** 1757–1867 (2007).
4. Päs, H. & Rodejohann, W. Neutrinoless double beta decay. *New J. Phys.* **17,** 115010 (2015).
5. Agostini, M. *et al.* Results on neutrinoless double-β decay of ^{76}Ge from phase I of the Gerda experiment. *Phys. Rev. Lett.* **111,** 122503 (2013).
6. Cuesta, C. *et al.* Status of the Majorana demonstrator. *AIP Conf. Proc.* **1686,** 020005 (2015).
7. Alfonso, K. *et al.* Search for neutrinoless double-beta decay of ^{130}Te with CUORE-0. *Phys. Rev. Lett.* **115,** 102502 (2015).
8. Andringa, S. *et al.* Current status and future prospects of the SNO+ experiment. *Adv. High Energy Phys.* **2016,** 6194250 (2016).
9. Gando, A. *et al.* Search for Majorana neutrinos near the inverted mass hierarchy region with KamLAND-Zen. *Phys. Rev. Lett.* **117,** 082503 (2016).
10. Albert, J. B. *et al.* Search for Majorana neutrinos with the first two years of EXO-200 data. *Nature* **510,** 229–234 (2014).
11. Martin-Albo, J. *et al.* Sensitivity of NEXT-100 to neutrinoless double beta decay. *J. High Energ. Phys.* **1605,** 159 (2016).
12. Mount, B. J., Redshaw, M. & Myers, E. G. Double-β-decay Q values of ^{74}Se and ^{76}Ge. *Phys. Rev. C* **81,** 032501 (2010).
13. Ackermann, K.-H. *et al.* The GERDA experiment for the search of $0\nu\beta\beta$ decay in ^{76}Ge. *Eur. Phys. J. C* **73,** 2330 (2013).
14. Heusser, G. Low-radioactivity background techniques. *Annu. Rev. Nucl. Part. Sci.* **45,** 543–590 (1995).
15. Klapdor-Kleingrothaus, H. V. *et al.* Search for neutrinoless double beta decay with enriched ^{76}Ge in Gran Sasso 1990–2003. *Phys. Lett. B* **586,** 198–212 (2004).
16. Aalseth, C. E. *et al.* IGEX ^{76}Ge neutrinoless double beta decay experiment: prospect for next generation experiments. *Phys. Rev. D* **65,** 092007 (2002).
17. Agostini, M. *et al.* Production, characterization and operation of ^{76}Ge enriched BEGe detectors in GERDA. *Eur. Phys. J. C* **75,** 39 (2015).
18. Agostini, M. *et al.* The background in the $0\nu\beta\beta$ experiment GERDA. *Eur. Phys. J. C* **74,** 2764 (2014).
19. Agostini, M. *et al.* Upgrade of the GERDA experiment. In *Proc. Sci. TIPP2014* 109, https://pos.sissa.it/archive/conferences/213/109/TIPP2014_109.pdf (2014).
20. Riboldi, S. *et al.* Cryogenic readout techniques for germanium detectors. In *Proc. 2015 4th Int. Conf. on Adv. in Nucl. Instrum. Meas. Methods and their Appl. (AMIMMA)* http://ieeexplore.ieee.org/document/7465549 (2015).
21. Agostini, M. *et al.* LArGe: active background suppression using argon scintillation for the GERDA $0\nu\beta\beta$-experiment. *Eur. Phys. J. C* **75,** 506 (2015).
22. Janicskó Csáthy, J. *et al.* Optical fiber read-out for liquid argon scintillation light. Preprint at http://arXiv.org/abs/1606.04254 (2016).
23. Freund, K. *et al.* The performance of the Muon Veto of the GERDA experiment. *Eur. Phys. J. C* **76,** 298 (2016).
24. Agostini, M., Pandola, L. & Zavarise, P. Off-line data processing and analysis for the GERDA experiment. *J. Phys. Conf. Ser.* **368,** 012047 (2012).
25. Agostini, M. *et al.* GELATIO: a general framework for modular digital analysis of high-purity Ge detector signals. *J. Instrum.* **6,** P08013 (2011).
26. Agostini, M. *et al.* Improvement of the energy resolution via an optimized digital signal processing in Gerda phase I. *Eur. Phys. J. C* **75,** 255 (2015).
27. Agostini, M. *et al.* Results on $\beta\beta$ decay with emission of two neutrinos or majorons in ^{76}Ge from Gerda phase I. *Eur. Phys. J. C* **75,** 416 (2015).
28. Agostini, M. *et al.* Pulse shape discrimination for GERDA phase I data. *Eur. Phys. J. C* **73,** 2583 (2013).
29. Budjáš, D. *et al.* Pulse shape discrimination studies with a broad-energy germanium detector for signal identification and background suppression in the Gerda double beta decay experiment. *J. Instrum.* **4,** P10007 (2009).
30. Agostini, M. *et al.* Signal modeling of high-purity Ge detectors with a small read-out electrode and application to neutrinoless double beta decay search in ^{76}Ge. *J. Instrum.* **6,** P03005 (2011).
31. Wagner, V. *Pulse Shape Analysis for the GERDA Experiment to Set a New Limit on the Half-life of $0\nu\beta\beta$ Decay of ^{76}Ge.* PhD thesis, MPI-K and Univ. Heidelberg (2016); http://www.ub.uni-heidelberg.de/archiv/22621 (2017).

32. Kirsch, A. *Search for the Neutrinoless Double β-decay in* GERDA *Phase I Using a Pulse Shape Discrimination Technique*. PhD thesis, MPI-K and Univ. Heidelberg http://www.ub.uni-heidelberg.de/archiv/17149 (2014).
33. Bruyneel, B., Birkenbach, B. & Reiter, P. Pulse shape analysis and position determination in segmented HPGe detectors: the AGATA detector library. *Eur. Phys. J. A* **52,** 70 (2016).
34. Agostini, M. *et al.* Limit on neutrinoless double beta decay of ^{76}Ge by GERDA. *Phys. Procedia* **61,** 828–837 (2015).
35. Menéndez, J. *et al.* Disassembling the nuclear matrix elements of the neutrinoless beta beta decay. *Nucl. Phys. A* **818,** 139–151 (2009).
36. Horoi, M. & Neacsu, A. Shell model predictions for ^{124}Sn double-β decay. *Phys. Rev. C* **93,** 024308 (2016).
37. Barea, J., Kotila, J. & Iachello, F. $0\nu\beta\beta$ and $2\nu\beta\beta$ nuclear matrix elements in the interacting boson model with isospin restoration. *Phys. Rev. C* **91,** 034304 (2015).
38. Hyvärinen, J. & Suhonen, J. Nuclear matrix elements for $0\nu\beta\beta$ decays with light or heavy Majorana-neutrino exchange. *Phys. Rev. C* **91,** 024613 (2015).
39. Šimkovic, F. *et al.* $0\nu\beta\beta$ and $2\nu\beta\beta$ nuclear matrix elements, quasiparticle random-phase approximation, and isospin symmetry restoration. *Phys. Rev. C* **87,** 045501 (2013).
40. López Vaquero, N., Rodriguez, T. R. & Egido, J. L. Shape and pairing fluctuation effects on neutrinoless double beta decay nuclear matrix elements. *Phys. Rev. Lett.* **111,** 142501 (2013).
41. Yao, J. *et al.* Systematic study of nuclear matrix elements in neutrinoless double-beta decay with a beyond-mean-field covariant density functional theory. *Phys. Rev. C* **91,** 024316 (2015).

Publisher's note: Springer Nature remains neutral with regard to jurisdictional claims in published maps and institutional affiliations. Correspondence and requests for materials should be addressed to the GERDA Collaboration (gerda-eb@mpi-hd.mpg.de).

Reviewer Information *Nature* thanks P. Barbeau, L. Canonica and the other anonymous reviewer(s) for their contribution to the peer review of this work.

The GERDA Collaboration

M. Agostini[1], M. Allardt[2], A. M. Bakalyarov[3], M. Balata[1], I. Barabanov[4], L. Baudis[5], C. Bauer[6], E. Bellotti[7,8], S. Belogurov[4,9], S. T. Belyaev[3]‡, G. Benato[5], A. Bettini[10,11], L. Bezrukov[4], T. Bode[12], D. Borowicz[13,14], V. Brudanin[14], R. Brugnera[10,11], A. Caldwell[15], C. Cattadori[8], A. Chernogorov[9], V. D'Andrea[1], E. V. Demidova[9], N. Di Marco[1], A. di Vacri[1], A. Domula[2], E. Doroshkevich[4], V. Egorov[14], R. Falkenstein[16], O. Fedorova[4], K. Freund[16], N. Frodyma[13], A. Gangapshev[4,6], A. Garfagnini[10,11], C. Gooch[15], P. Grabmayr[16], V. Gurentsov[4], K. Gusev[3,12,14], J. Hakenmüller[6], A. Hegai[16], M. Heisel[6], S. Hemmer[10,11], W. Hofmann[6], M. Hult[17], L. V. Inzhechik[4], J. Janicskó Csáthy[12], J. Jochum[16], M. Junker[1], V. Kazalov[4], T. Kihm[6], I. V. Kirpichnikov[9], A. Kirsch[6], A. Kish[5], A. Klimenko[6,14], R. Kneißl[15], K. T. Knöpfle[6], O. Kochetov[14], V. N. Kornoukhov[4,9], V. V. Kuzminov[4], M. Laubenstein[1], A. Lazzaro[12], V. I. Lebedev[3], B. Lehnert[2], H. Y. Liao[15], M. Lindner[6], I. Lippi[11], A. Lubashevskiy[6,14], B. Lubsandorzhiev[4], G. Lutter[17], C. Macolino[1], B. Majorovits[15], W. Maneschg[6], E. Medinaceli[10,11], M. Miloradovic[5], R. Mingazheva[5], M. Misiaszek[13], P. Moseev[4], I. Nemchenok[14], D. Palioselitis[15], K. Panas[13], L. Pandola[18], K. Pelczar[13], A. Pullia[19], S. Riboldi[19], N. Rumyantseva[14], C. Sada[10,11], F. Salamida[8], M. Salathe[6], C. Schmitt[16], B. Schneider[2], S. Schönert[12], J. Schreiner[6], O. Schulz[15], A.-K. Schütz[16], B. Schwingenheuer[6], O. Selivanenko[4], E. Shevchik[14], M. Shirchenko[14], H. Simgen[6], A. Smolnikov[6,14], L. Stanco[11], L. Vanhoefer[15], A. A. Vasenko[9], A. Veresnikova[4], K. von Sturm[10,11], V. Wagner[6], M. Walter[5], A. Wegmann[6], T. Wester[2], C. Wiesinger[12], M. Wojcik[13], E. Yanovich[4], I. Zhitnikov[14], S.V. Zhukov[3], D. Zinatulina[14], K. Zuber[2] & G. Zuzel[13]

[1]INFN Laboratori Nazionali del Gran Sasso and Gran Sasso Science Institute, Assergi, Italy. [2]Institut für Kern- und Teilchenphysik, Technische Universität Dresden, Dresden, Germany. [3]National Research Centre "Kurchatov Institute", Moscow, Russia. [4]Institute for Nuclear Research of the Russian Academy of Sciences, Moscow, Russia. [5]Physik Institut der Universität Zürich, Zurich, Switzerland. [6]Max-Planck-Institut für Kernphysik, Heidelberg, Germany. [7]Dipartimento di Fisica, Università Milano Bicocca, Milan, Italy. [8]INFN Milano Bicocca, Milan, Italy. [9]Institute for Theoretical and Experimental Physics, Moscow, Russia. [10]Dipartimento di Fisica e Astronomia dell 'Università di Padova, Padua, Italy. [11]INFN Padova, Padua, Italy. [12]Physik Department and Excellence Cluster Universe, Technische Universität München, Germany. [13]Institute of Physics, Jagiellonian University, Cracow, Poland. [14]Joint Institute for Nuclear Research, Dubna, Russia. [15]Max-Planck-Institut für Physik, Munich, Germany. [16]Physikalisches Institut, Eberhard Karls Universität Tübingen, Tübingen, Germany. [17]European Commission, JRC-Geel, Geel, Belgium. [18]INFN Laboratori Nazionali del Sud, Catania, Italy. [19]Dipartimento di Fisica, Università degli Studi di Milano e INFN Milano, Milan, Italy. ‡Deceased.

METHODS

Statistical analysis. This section discusses the statistical analysis of the GERDA data. In particular, the procedures to derive the limit on $T^{0\nu}_{1/2}$, the median sensitivity of the experiment and the treatment of systematic uncertainties are described.

A combined analysis of data from Phase I and II is performed by fitting simultaneously the six data sets of Table 1. The parameter of interest for this analysis is the strength of a possible $0\nu\beta\beta$ decay signal: $\mathcal{S} = 1/T^{0\nu}_{1/2}$. The number of expected $0\nu\beta\beta$ events in the ith data set $\mathcal{D}_i$ as a function of $\mathcal{S}$ is given by:

$$\mu^S_i = \ln2(N_A/m_a)\epsilon_i\mathcal{E}_i\mathcal{S} \tag{2}$$

where N_A is Avogadro's number, ϵ_i the global signal efficiency of the ith data set, $\mathcal{E}_i$ the exposure and m_a the molar mass. The exposure quoted is the total detector mass multiplied by the data-taking time. The global signal efficiency accounts for the fraction of ^{76}Ge in the detector material, the fraction of the detector active volume, the efficiency of the analysis cuts, the fractional live time of the experiment and the probability that $0\nu\beta\beta$ decay events in the active detector volume have a reconstructed energy at $Q_{\beta\beta}$. The total number of expected background events as a function of the background index BI_i is:

$$\mu^B_i = \mathcal{E}_i BI_i \Delta E \tag{3}$$

where $\Delta E = 240\,keV$ is the width of the energy region around $Q_{\beta\beta}$ used for the fit.

Each data set $\mathcal{D}_i$ is fitted with an unbinned likelihood function assuming a Gaussian distribution for the signal and a flat distribution for the background:

$$\mathcal{L}_i(\mathcal{D}_i|\mathcal{S}, BI_i, \theta_i) = $$
$$\prod_{j=1}^{N^{obs}_i} \frac{1}{\mu^B_i + \mu^S_i}\left[\mu^B_i\frac{1}{\Delta E} + \mu^S_i\frac{1}{\sqrt{2\pi}\,\sigma_i}\exp\left(\frac{-(E_j - Q_{\beta\beta} - \delta_i)^2}{2\sigma^2_i}\right)\right] \tag{4}$$

where E_j are the individual event energies, N^{obs}_i is the total number of events observed in the ith data set, $\sigma_i = FWHM_i/(2\sqrt{2\ln2})$ is the energy resolution and δ_i is a possible systematic energy offset. The parameters with systematic uncertainties are indicated with $\theta_i = \{\varepsilon_i, \sigma_i, \delta_i\}$. The parameters $\mathcal{S}$ and BI_i are bound to positive values. The total likelihood is constructed as the product of all $\mathcal{L}_i$ weighted with the Poisson terms[42]:

$$\mathcal{L}(\mathcal{D}|\mathcal{S}, BI, \theta) = $$
$$\prod_i\left[\frac{e^{-(\mu^S_i + \mu^B_i)}(\mu^S_i + \mu^B_i)^{N^{obs}_i}}{N^{obs}_i!} \times \mathcal{L}_i(\mathcal{D}_i|\mathcal{S}, BI_i, \theta_i)\right] \tag{5}$$

where $\mathcal{D} = \{\mathcal{D}_1 \dots \mathcal{D}_i \dots\}$, $BI = \{BI_1 \dots BI_i \dots\}$ and $\theta = \{\theta_1 \dots \theta_i \dots\}$.

A frequentist analysis is performed using a two-sided test statistics[43] based on the profile likelihood $\lambda(\mathcal{S})$:

$$t_{\mathcal{S}} = -2\ln\lambda(\mathcal{S}) = -2\ln\frac{\mathcal{L}(\mathcal{S}, \widehat{\widehat{BI}}, \hat{\hat{\theta}})}{\mathcal{L}(\hat{\mathcal{S}}, \widehat{BI}, \hat{\theta})} \tag{6}$$

where $\widehat{\widehat{BI}}$ and $\hat{\hat{\theta}}$ in the numerator denote the value of the parameters that maximizes $\mathcal{L}$ for a fixed $\mathcal{S}$. In the denominator, $\hat{\mathcal{S}}$, $\widehat{BI}$ and $\hat{\theta}$ are the values corresponding to the absolute maximum likelihood.

The confidence intervals are constructed for a discrete set of values $\mathcal{S} \in \{\mathcal{S}_j\}$. For each $\mathcal{S}_j$, possible realizations of the experiments are generated via Monte Carlo according to the parameters of Table 1 and the expected number of counts from equations (2) and (3). For each realization $t_{\mathcal{S}_j}$ is evaluated. From the entire set the probability distribution $f(t_{\mathcal{S}}|\mathcal{S}_j)$ is calculated. The P value of the data for a specific $\mathcal{S}_j$ is computed as:

$$p_{\mathcal{S}_j} = \int_{t_{obs}}^{\infty} f(t_{\mathcal{S}}|\mathcal{S}_j)d(t_{\mathcal{S}_j}) \tag{7}$$

where t_{obs} is the value of the test statistics of the GERDA data for $\mathcal{S}_j$. The values of $p_{\mathcal{S}_j}$ are shown by the solid line in Extended Data Fig. 5. The 90% CL interval is given by all $\mathcal{S}_j$ values with $p_{\mathcal{S}_j} > 0.1$. Such an interval has the correct coverage by construction. The current analysis yields a one-sided interval, that is, a limit of $T^{0\nu}_{1/2} = 1/\mathcal{S} > 5.3 \times 10^{25}\,yr$.

The expectation for the frequentist limit (that is, the experimental sensitivity) was evaluated from the distribution of $p_{\mathcal{S}_j}$ built from Monte Carlo generated data sets with no injected signal ($\mathcal{S} = 0$). The distribution of $p_{\mathcal{S}_j}$ is shown in Extended Data Fig. 5: the dashed line is the median of the distribution and the colour bands indicate the 68% and 90% probability central intervals. The experimental sensitivity corresponds to the $\mathcal{S}$ value at which the median crosses the P-value threshold of 0.1: $T^{0\nu}_{1/2} > 4.0 \times 10^{25}\,yr$ (90% CL).

Systematics uncertainties are folded into the likelihood by varying the parameters θ_i in the fits and constraining them by adding to the likelihood multiplicative Gaussian penalty terms. The central values and the standard deviations of the penalty terms for ϵ_i and σ_i are taken from Table 1. The penalty term on δ_i has a central value equal to zero and standard deviation of $0.2\,keV$.

Instead of the two-sided test statistics, one can use a one-sided test statistic defined as[43]:

$$\tilde{t}_{\mathcal{S}} = \begin{cases} 0, & \hat{\mathcal{S}} > \mathcal{S} \geq 0 \\ -2\ln\lambda(\mathcal{S}), & \hat{\mathcal{S}} \leq \mathcal{S} \end{cases} \tag{8}$$

By construction $\tilde{t}_{\mathcal{S}} = 0$ for $\mathcal{S} = 0$ for all realizations and consequently $\mathcal{S} = 0$ is always included in the 90% CL interval, that is, the one-sided test statistic will always yield a limit. In our case the resulting limit would be 50% stronger. Similar to other experiments[9,10], we want to be able to detect a possible signal and thus we decided a priori to adopt the two-sided test statistic. It is noteworthy that, although the coverage of both test statistics is correct by construction, deciding which one to use according to the outcome of the experiment would result in the flip-flop issue discussed in ref. 44.

The statistical analysis is also performed within a Bayesian framework. The combined posterior probability density function (PDF) is calculated from the six data sets according to Bayes' theorem:

$$\mathcal{P}(\mathcal{S}, BI|\mathcal{D}, \theta) \propto \mathcal{L}(\mathcal{D}|\mathcal{S}, BI, \theta)\mathcal{P}(\mathcal{S})\prod_i\mathcal{P}(BI_i) \tag{9}$$

The likelihood $\mathcal{L}$ is given by equation (5), while $\mathcal{P}(\mathcal{S})$ and $\mathcal{P}(BI_i)$ are the prior PDFs for $\mathcal{S}$ and for the background indices, respectively. The one-dimensional posterior PDF $\mathcal{P}(\mathcal{S}|\mathcal{D}, \theta)$ of the parameter $\mathcal{S}$ of interest is derived by marginalization over all nuisance parameters BI. The marginalization is performed by the BAT toolkit[45] via a Markov chain Monte Carlo numerical integration. A flat PDF between 0 and $0.1\,counts\,keV^{-1}\,kg^{-1}\,yr^{-1}$ is considered as prior for all background indices. As in ref. 5, a flat prior distribution is taken for $\mathcal{S}$ between 0 and $10^{-24}\,yr^{-1}$, that is, all counting rates up to a maximum are considered to be equiprobable. The parameters θ in the likelihood $\mathcal{L}$ are fixed during the Bayesian analysis and the uncertainties are folded into the posterior PDF as last step by an integral average:

$$\langle\mathcal{P}(\mathcal{S}|\mathcal{D})\rangle = \int\mathcal{P}(\mathcal{S}|\mathcal{D}, \theta)\prod_i g(\theta_i)d\theta_i \tag{10}$$

with $g(\theta_i)$ being Gaussian distributions like for the frequentist analysis. The integration is performed numerically by a Monte Carlo approach.

The median sensitivity of the experiment in the case of no signal is $T^{0\nu}_{1/2} > 3.1 \times 10^{25}\,yr$ (90% CI). The posterior PDF $\langle\mathcal{P}(\mathcal{S}|\mathcal{D})\rangle$ for our data has an exponential shape with the mode at $\mathcal{S} = 0$. Its 90% probability quantile yields $T^{0\nu}_{1/2} > 3.5 \times 10^{25}\,yr$.
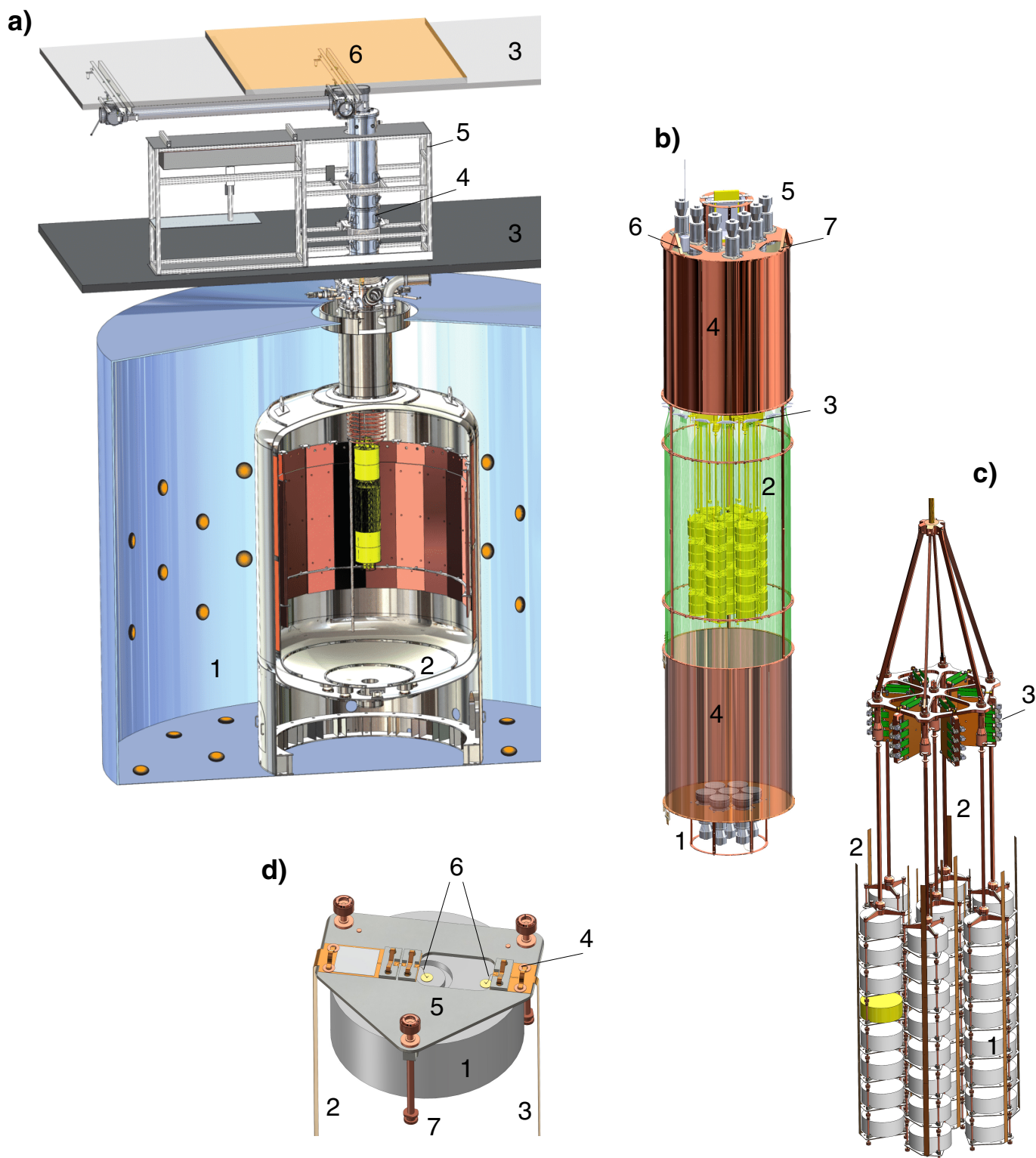
As in any Bayesian analysis, results depend on the choice of the priors. For our limit we assume all signal count rates to be a priori equiprobable. Alternative reasonable choices are for instance: equiprobable Majorana neutrino masses, which yields a prior proportional to $1/\sqrt{\mathcal{S}}$; or scale invariance in the counting rate, namely a flat prior in $\log(\mathcal{S})$. The limits derived with these assumptions are stronger (50% or more), since for both alternatives the prior PDFs increase the probability of low $\mathcal{S}$ values.

The systematic uncertainties weaken the limit on $\mathcal{S}$ by less than 1% both in the frequentist and Bayesian analysis. In general, the impact of systematic uncertainties on limits is marginal in the low-statistics regime that characterizes our experiment (see also ref. 46).

The limit derived from the GERDA data is slightly stronger than the median sensitivity. This effect is more relevant in the frequentist analysis as one would expect (see, for example, ref. 47 for a detailed discussion). The probability of obtaining a frequentist (Bayesian) limit stronger than the actual one is 33% (35%).

Data availability. All data generated during this analysis and shown in Figs 1–4 are available in ASCII format (CSV) as Source Data and from the GERDA home page (https://www.mpi-hd.mpg.de/gerda/public/index.html). For further information contact the GERDA Collaboration (gerda-eb@mpi-hd.mpg.de).

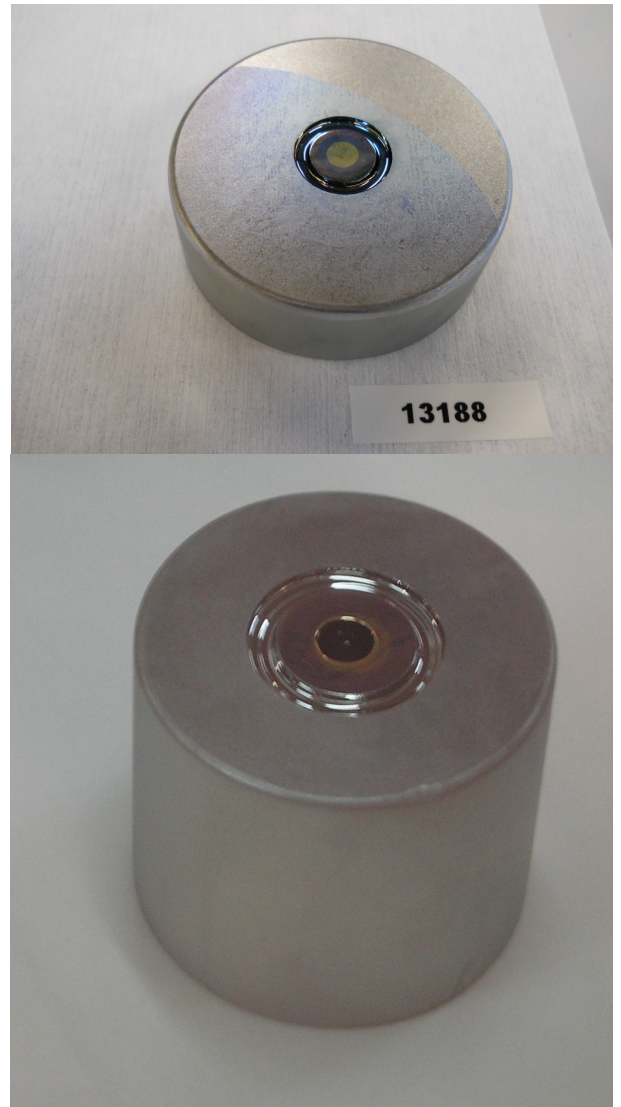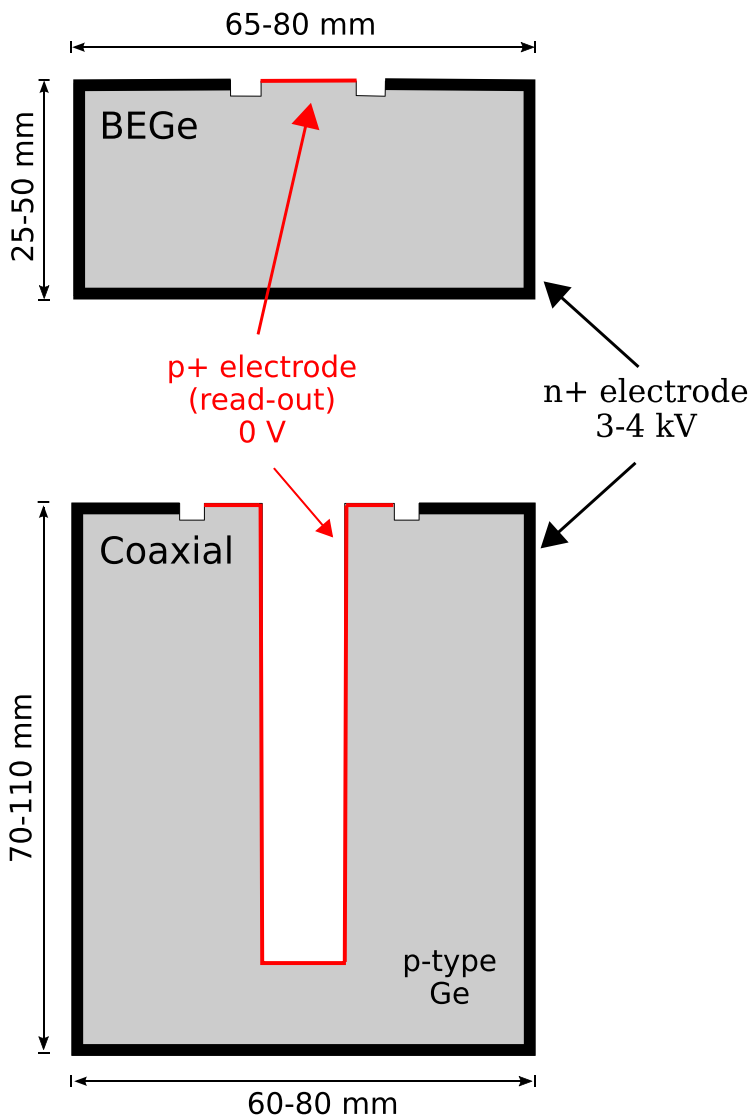42. Beringer, J. et al. Review of particle physics. Phys. Rev. D **86**, 010001 (2012).
43. Cowan, G. et al. Asymptotic formulae for likelihood-based tests of new physics. Eur. Phys. J. C **71**, 1554 (2011).
44. Feldman, G. J. & Cousins, R. D. Unified approach to the classical statistical analysis of small signals. Phys. Rev. D **57**, 3873–3889 (1998).
45. Caldwell, A., Kollar, D. & Kröninger, K. BAT — the Bayesian Analysis Toolkit. Comput. Phys. Commun. **180**, 2197–2209 (2009).
46. Cousins, R. & Highland, V. Incorporating systematic uncertainties into an upper limit. Nucl. Instrum. Methods Phys. Res. A **320**, 331–335 (1992).
47. Biller, S. V. & Oser, S. M. Another look at confidence intervals: proposal for a more relevant and transparent approach. Nucl. Instrum. Methods Phys. Res. A **774**, 103–119 (2015).

Extended Data Figure 1 | GERDA Phase II experimental set-up.
a, Overview. 1, water tank with muon veto system PMTs (590 m³, diameter 10 m); 2, LAr cryostat (64 m³, diameter 4 m); 3, floor and roof of clean room; 4, lock; 5, glove box; 6, plastic muon veto system. **b**, LAr veto system: 1, bottom plate (diameter 49 cm) with 7 3-inch PMTs (R11065-10/20 MOD) with low radioactivity of U and Th (<2 mBq per PMT); 2, fibre curtain (height 100 cm) coated with wavelength shifter; 3, optical couplers and SiPMs; 4, thin-walled (0.1 mm) Cu cylinders (height 60 cm) covered with a Tyvek reflector on the inside; 5, top plate with properties as bottom plate 1 except for 9 3-inch PMTs; 6, calibration source entering slot in top plate; 7, slot for second of three calibration sources. **c**, Detector array. 1, Ge detectors arranged in 7 strings; 2, flexible bias and readout cables; 3, amplifiers. **d**, Detector module, view from bottom. 1, BEGe diode; 2, signal cable; 3, high voltage cable. 2 and 3 are attached by 4, bronze clamps to 5, silicon support plate; 6, bond wire connections from diode to signal and high voltage cable; 7, Cu support rods.
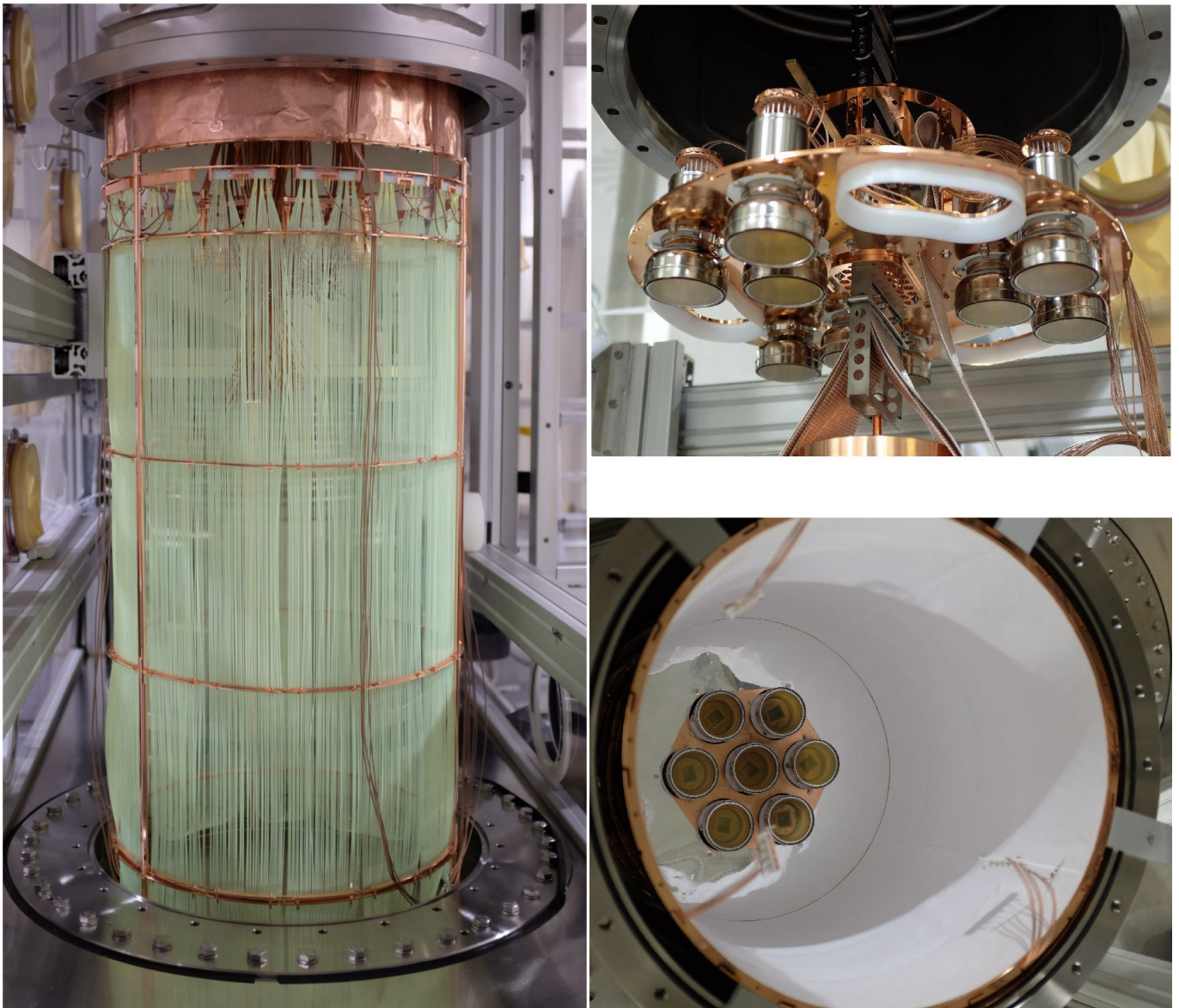
65-80 mm

BEGe

25-50 mm

p+ electrode
(read-out)
0 V

n+ electrode
3-4 kV

Coaxial

70-110 mm

p-type
Ge

60-80 mm

13188

Extended Data Figure 2 | Detector types. Cross-section through the germanium detector types (left) and the corresponding photographs of them (right). The p+ electrode is made by a ~0.3 μm thin boron implantation. The n+ el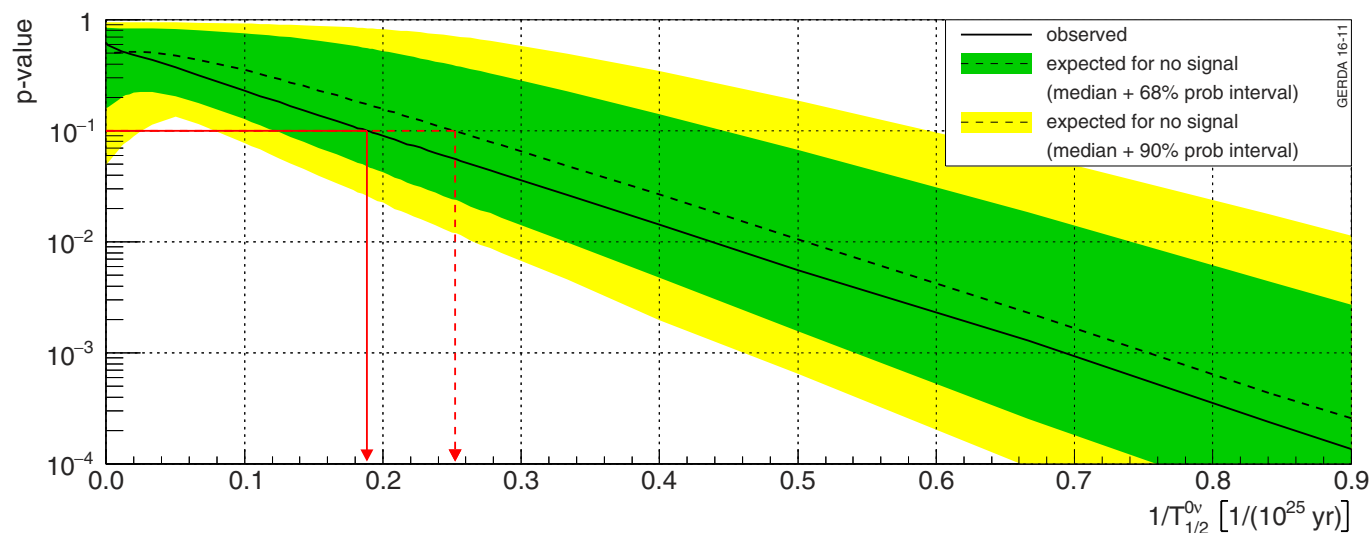ectrode is a 1 to 2 mm thick lithium diffusion layer and is biased with up to +4,500 V. The electric field drops to zero in the n+ layer, and hence energy depositions in this fraction of the volume do not create a readout signal. The p+ electrode is connected to a charge sensitive amplifier.

Extended Data Figure 3 | Germanium detector array. Photograph of the assembled detector array, with a string of coaxial detectors on the left, and strings of BEGe detectors at middle and right. Each string is enclosed by a cylindrical nylon shroud covered with a wavelength shifter.

Extended Data Figure 4 | Liquid argon veto set-up. Photographs of the LAr veto system: left, fibre curtain with SiPM readout at the top; right, top and bottom arrangement of PMTs.

Extended Data Figure 5 | Frequentist hypothesis test. *P* value for the hypothesis test as a function of the inverse half-life $1/T^{0\nu}_{1/2}$ according to equation (7). The colour bands indicate the spread of the *P*-value distributions for many Monte Carlo realizations according to the GERDA parameters (with no signal): green and yellow show the central 68% and 90% probability intervals, respectively. The dashed black line represents the median of the distribution; the *P* value for the GERDA data is shown as a solid black line. The red arrows indicate the results at 90% confidence level, that is, a *P* value of 0.1: the limit for $T^{0\nu}_{1/2}(^{76}\text{Ge}) > 5.3 \times 10^{25}$ yr (full red arrow), and the median sensitivity for $T^{0\nu}_{1/2}(^{76}\text{Ge}) > 4.0 \times 10^{25}$ yr (dashed red arrow). For a detailed discussion of their computation, see Methods.